Article

Shear Modulus of Carbonate Sand-Silt Mixture with THF Hydrate

Yuzhe Ren [1], C.F. Chiu [2],* , Lu Ma [3], Y.P. Cheng [4], Litong Ji [5], and Chao Jiang [1]

[1] Key Laboratory of Ministry of Education for Geomechanics and Embankment Engineering, Hohai University, Nanjing 210098, China; yuzherenyuzhe@outlook.com(Yuzhe Ren); jc13655196074@outlook.com(Chao Jiang)

[2] Guangdong Engineering Center for Structure Safety and Health Monitoring, Shantou University, Shantou 515063, China; acf_chiu@stu.edu.cn

[3] College of Architecture, Anhui Science and Technology University, Bengbu 232002, China; mal@ahstu.edu.cn

[4] Department of Civil, Environmental and Geomatic Engineering, University College London, UK; yi.cheng@ucl.ac.uk

[5] Nanjing TKA Technology, Nanjing 210005, China; sales@tkatest.com

* Correspondence: acf_chiu@stu.edu.cn

Abstract: Maximum shear modulus (G_{max}) is an important factor determining soil deformation and closely related to engineering safety and seafloor stability. In this study, a series of bender element tests was carried out to investigate the G_{max} of hydrate bearing Carbonate sand (CS)-silt mixture. The soil mixture adopted a CS : silt ratio of 1:4 by weight to mimic the fine-grained deposit of South China Sea (SCS). Tetrahydrofuran (THF) was used to form hydrate. Special specimen preparation procedures were adopted to form THF hydrate inside the intra-particle voids of CS. The test results indicate that hydrate contributes to a significant part in the skeleton stiffness of the hydrate bearing CS-silt mixture and its G_{max} at 5% hydrate saturation (S_h) is 4 to 6 times that of the host soil mixture. Such stiffness enhancement at the low S_h may be related to the cementation hydrate morphology. However, G_{max} of the hydrate bearing CS-silt mixture is also sensitive to the effective stress for S_h ranging between 5% and 31%, implying that the frame-supporting hydrate morphology also plays a key role in the skeletal stiffness of the soil mixture. Neither the existing cementation models nor the theoretical frame-supporting, i.e. Biot-Gassmann theory by Lee (BGTL) could alone give a satisfactory prediction of the test results. Thus, further theoretical study involving a combination of cementation and frame-supporting models is essential to understand the effects of complicated hydrate morphologies on the stiffness of soil with substantial amount of intra-particle voids.

Keywords: tetrahydrofuran hydrate; carbonate sand; silt; maximum shear modulus; bender element test

1. Introduction

Gas hydrate is emerging as one of the future energy sources, but its dissociation can cause significant environmental hazards, such as release of methane (a potent greenhouse gas), instability of seafloor, etc. Past studies have revealed that hydrate morphology is one of the crucial factors governing the mechanical behaviour of hydrate bearing sediments. In coarse-grained soil, the following three hydrate morphologies are commonly assumed: pore-filling, load-bearing and cementation [1]. As hydrate formation in sediments depends on many factors, such as geological conditions and fluid conductivity of the sediments, transportation mechanism of gas, etc., many complex hydrate morphologies can exist, like segregated veins, nodules and lens in fine-grained soil, heterogeneous hydrate patches in coarse-grained soil under high effective stress [2,3]. Besides, it is a significantly difficult task to identify the occurrence of paleo-gas hydrate in fossil

sediments. Based on long-term field data, recent studies have shown that clathrite-like structures and geo-chemical properties in pore-water are useful indicators that provide useful information for understanding the formation and dissociation of gas hydrate [4,5]. Recent field explorations in the South China Sea (SCS) have reported that high methane hydrate saturation can be found in the fine-grained sediments containing foraminifera (carbonate fossils containing significant proportion of intra-particle voids) [6]. Compared with the small inter-particle voids of the fine-grained soil matrix, hydrates tend to form in the larger intra-particle voids of foraminifera. As such the distribution of hydrates is heterogeneous depending on the spatial variability of foraminifera instead of evenly distributed in the voids.

Different laboratory methods have been adopted to form hydrate in soil specimens resulting in different hydrate morphologies, e.g. excess-gas method [7,8], excess-water method [9,10], ice-seed method [11,12], etc. However, two other methods are used for fine-grained soils of low permeability. In the first method, under high pressure and low temperature, methane gas was injected and reacted with ice powder with an average particle size of 250 μm to form hydrate powder. Then, it was mixed with fine-grained soil [13-15]. However, no bonding is formed between hydrate and soil particles in this method. This study adopted the second method where Tetrahydrofuran (THF) was used to replace methane gas [16-18]. THF hydrate is often adopted as a good substitute for methane hydrate owing to the similarity in mechanical and thermal properties. As THF is miscible with water at room temperature, it is easier to control the hydrate saturation and its distribution by adding the estimated amount of THF/water solution to the desired location of the specimen. The objective of the study is to model the hydrate accumulation inside the inter-particle voids of CS rather than the field hydrate formation process. Only CS was soaked in the THF/water solution to achieve this ends and details of laboratory procedures will be presented in the next section. It should be noted that THF hydrate discomposes into liquid without gas during dissociation, thus one of the limitations is no gas dissociation can be modelled from THF hydrate.

Deformation and shear strength of soil are closely related to the safety of engineering structures and seafloor stability during hydrate exploitation. Thus, mechanical properties of hydrate bearing soils have been reported in the past literature, e.g. the stress-strain behaviour and shear strength of hydrate bearing sand [19], the dynamic shear modulus and damping ratio of hydrate bearing sand [20], the effects of hydrate on the rheological properties of mudflow [21], shear wave velocity and maximum shear modulus (G_{max}) of hydrate bearing sand [22], etc.. Clayton et al. [22] conducted a series of resonant column tests on sand-sized geomaterials. The results showed that cementation morphology has more significant influence on the shear moduli of the host sand than pore-filling morphology. Similarly, Liu et al. [20] carried out resonant column tests on THF hydrate bearing sand. The results revealed that effective stress and hydrate can enhance the shear modulus, while high hydrate saturation would suppress its enhancement. However, the effects of hydrate accumulated inside the intra-particle voids on the soil stiffness of fine-grained sediments with carbonate fossils are not well understood. In this study, special laboratory procedures were applied to form hydrate in the intra-particle voids of the CS-silt mixture. Bender element test was used to study G_{max} of the THF hydrate bearing CS-silt mixture with the hydrate filling the intra-particle voids. The effects of this type of hydrate morphology on G_{max} of the fine-grained soil mixture have been rarely reported in the literature. Furthermore, the effects of hydrate on the soil stiffness were compared and discussed using the theoretical frame-supporting and cementation models.

2. Materials and Methods

The tested soil mixture was formed by mixing a carbonate sand (CS) and a non-plastic silt in a ratio of 1:4 by dry weight to mimic the fine-grained sediment in SCS. The CS is a marine sediment consisting of angular and shelly carbonate particles, which

has similar chemical compositions and mechanical properties with foraminifera. As CS particles contain a substantial proportion of intra-particle voids, one of the objectives for this study to model the hydrate accumulation in the intra-particle voids of the tested soil mixture. The silt is a crushed quartz. Table 1 summarises the basic physical properties of the tested soils. The average particle size (d_{50}) and effective particle size (d_{10}) of the soil mixture are 50 and 17 μm, respectively. Figure 1 shows the particle size distribution (PSD) for CS, silt and the CS-silt mixture. The PSDs of two fine-grained sediment samples taken from SCS [23] are also presented in the figure for comparison. The CS-silt mixture is a gap-graded soil and the range of particle sizes is consistent with that of SCS sediments. Despite the tested soil mixture does not contain any fraction of clay, the fines content is similar to the marine sediment samples taken from the SCS. Ma et al. [24] found that the fines play the dominant role in the soil matrix of the mixture if CS content is less than 60%. To focus on the effects of intra-particle voids of CS on the stiffness of the CS-silt mixture, only fines content but not the soil plasticity was modelled correctly in this study. Moreover, the permeability of soil decreases with increasing clay content. To minimise the effects of permeability of soil on the hydrate formation in the specimen, clay was not included in the soil mixture. Further study will be required to investigate soil mixtures with some fractions of clay which represent more closely the natural marine sediments.
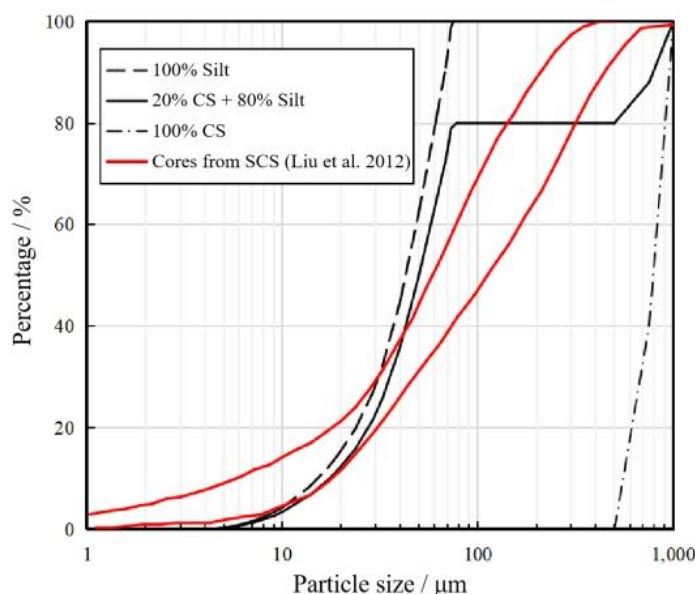


Figure 1. Particle size distribution of CS-silt mixture.

Table 1. Physical properties of tested soils.

Soils	Specific gravity G_s	Diameter range (mm)	d_{50} (mm)	Maximum void ratio	Minimum void ratio
Non-plastic silt	2.63	< 0.075	0.043	1.176	0.560
Carbonate sand (CS)	2.77	0.5 –1.0	0.750	1.336	0.957
Soil mixture	—	< 0.075, 0.5 –1.0	0.050	1.010	0.476

THF was used in this study to form hydrate in the soil specimens. The following procedures were used to ensure the hydrate accumulation in the intra-particle voids of specimens. A given weight of oven-dried samples of CS was first soaked inside a THF/water solution (21% THF by volume) under vacuum to saturate the intra-particle

voids. After soaking, the weight of wetted CS was carefully measured to determine the weight of THF/water solution used in the soil specimen. The wetted CS was mixed thoroughly with the oven-dried silt. Then, the soil mixture was compacted on the pedestal of triaxial test device to three different initial void ratios as shown in Table 2 using the wet tamping method. Hydrate saturation (S_h) shown in Table 2 is defined as the ratio of volume of hydrate to the volume of void. In the solution consisting of 21% THF and 79% water by volume, all solution will form hydrate if the soil specimen is subjected to appropriate high pressure and low temperature conditions [25]. In other words, the hydrate bearing specimens are dry specimens. The volume of hydrate is determined as the ratio of the weight of THF/water solution of in the soil specimen to the density of THF hydrate, which is taken as 0.981×10^3 kg/m^3 [26]. By adjusting the proportion of CS soaked in the THF/water solution, the percentage of intra-particle voids filled with hydrate was controlled between 25% and 100%. Besides, three control specimens without hydrate ($S_h = 0$) were compacted to the target initial void ratios as shown in Table 2.

To verify the intra-particle voids of CS were saturated by the THF/water solution after soaking, a THF/water solution-soaked CS specimen was scanned by micro-CT equipped with a high-resolution X-ray tube (Type: XTH225/320 LC from Nikon). A CT image of a typical cross-section of CS specimen is as shown in Figure 2. The grey, yellow and black colour represent soil particle, THF/water solution and air, respectively. It is depicted THF/water solution is either filled inside the intra-particle voids or on the surface of CS particles. After mixing THF/water-soaked CS with dry silt, it is postulated the THF/water solution remained inside the intra-particle voids and on the surface of CS particles of the CS-silt specimens. Nikitin et al. [27] observed that there was inevitable water migration during the methane hydrate formation due to cryogenic suction. However, the influence of excess-gas method in their study on water migration was omitted, in which multi-phase flow may cause water movement. In this study, it is assumed that there was negligible water migration in the specimens during hydrate formation when the temperature decreased below 0 °C. Hence, it is reasonable to assume hydrate was formed in the intra-particle voids and inter-particle voids adjacent to CS particles as shown in Figure 3. The accumulation of hydrate inside the intra-particle voids of CS-silt specimen agrees well with that observed in the field samples of hydrate bearing sediment containing carbonate fossils taken from SCS [28].
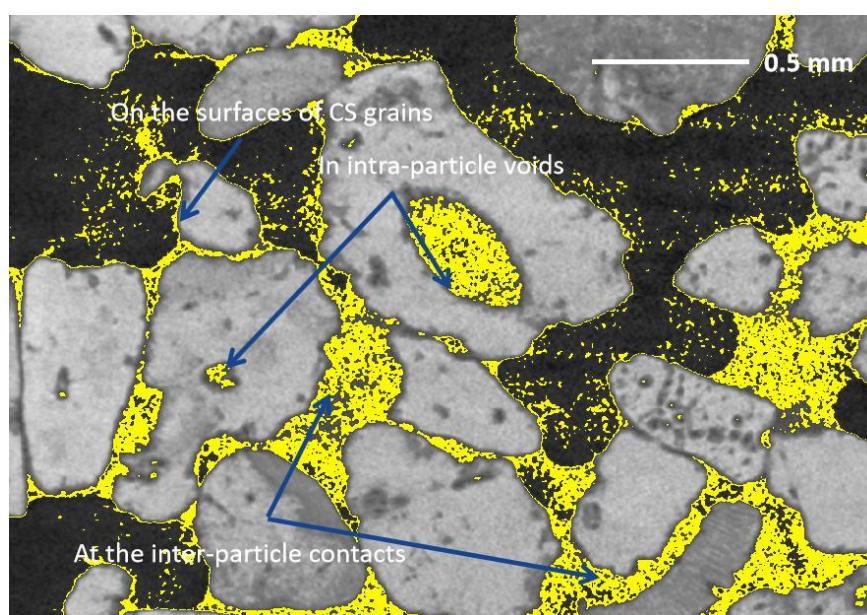
Figure 2. Micro-CT image of distribution of THF/water solution in CS specimen.
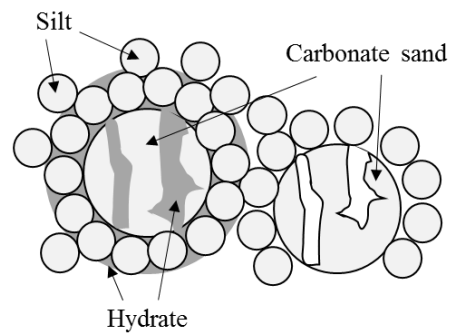
Figure 3. Proposed hydrate morphology of CS-silt mixture

Maximum shear modulus (G_{max}) was measured using a temperature controlled triaxial test apparatus with a pair of bender elements installed at the top cap and bottom pedestals of the triaxial cell as shown in Figures 4 (a) and (b), in which dimethyl silicone oil was chosen as the medium to provide confining pressure and heat exchange. The experimental system was designed by Nanjing TKA Technology Co., Ltd., which consists of a triaxial apparatus, two water pumps, a thermal controller, a temperature sensor, a wave generator, a power amplifier, an oscilloscope, a signal amplifier and a linear power supply. It is worth noting that the bender element on the top cap should be aligned carefully to keep it parallel to another one on the bottom pedestal for the accuracy of the shear wave measurement. In this study only the time difference between the peak emitted wave and that of received wave was chosen to calculate the shear wave velocity (v_s) in this study. Details of interpretation of bender element signals have been reported in Ji et al. [29]. It should be noted that it is also possible to measure the damping ratio (ζ) of soil using the bender element test [30], i.e. the viscous behaviour of soil. In general, ζ is determined by viscoelasticity methods recommended in Sodeifian [31] and Liu et al. [20]. Cheng and Leong [30] proposed that ζ can be measured by applying the Hilbert transform method to the bender element test results. Although, bender element signals can be processed to study the viscoelastic behaviour of soil, this study has focused only on the small strain stiffness, i.e. G_{max} of THF hydrate bearing soil.
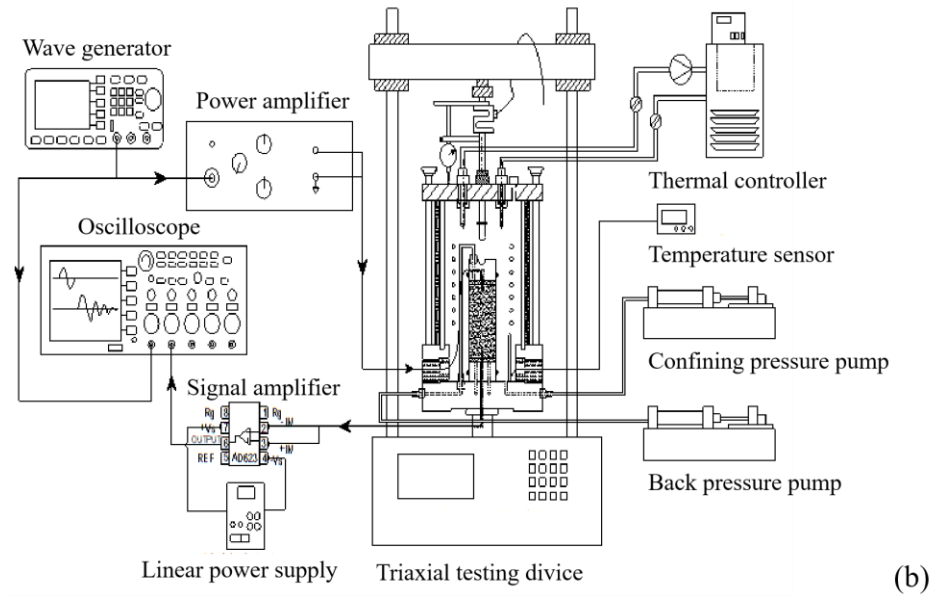
Figure 4. (*a*) Photo and (*b*) schematic setup of bender element test apparatus.

Table 2. Test conditions.

Specimen ID	Initial void ratio e_0	Percentage of intra-particle voids filled with hydrate	Effective void ratio e'	Hydrate saturation S_h (%)	Effective confining stress σ_c' (kPa)
1	0.799	0	0.799	0	100, 200, 300, 400
2	0.799	100	0.510	24	100, 300, 500, 800
3[a]	0.733	0	0.733	0	100. 200, 300, 400
4	0.733	25	0.672	5	100, 300, 500
5	0.733	50	0.593	12	100, 300, 500, 800
6[a]	0.733	100	0.447	27	100, 300, 500, 800
7	0.666	0	0.666	0	100, 200, 300, 400
8	0.666	100	0.381	31	100, 300, 500, 800

[a] from Ji et al. [29].

3. Results and Discussion

Table 2 shows that eight specimens were tested in this study. As the control of high pressure and low temperature was time-consuming, only two replicated tests have been carried out for each specimen ID 1 and 2 to verify the reproducibility of consistent specimens and reliability of test data. Figure 5 shows the measured shear wave velocity against the effective confining pressure for the host soil mixture (S_h = 0) and those with S_h ranging between 24% and 31%. The test results of six specimen ID are depicted in the figure for e_0 ranging from 0.666 to 0.799 and effective confining pressure ranging from 100 to 800 kPa. The measured v_s of specimen ID 1 and 2 (e_0 = 0.799) are the average values of two replicated tests. It is found that the measurements are within ±8% and ±5% of the average values for specimen ID 1 and 2, respectively. Those of remaining four specimens are measurements of single test. The test results of two other fine-grained soils are also shown in the figure for comparison [32,33]. Hardin and Richart [34] suggested that v_s can be related to the effective stress by the following equation:

$$v_s = a\left(\sigma_c{'}\right)^b \tag{1}$$

where $\sigma_c{'}$ is the effective confining stress, a and b are two fitting parameters. b reflects the sensitivity of effective stress on v_s. Eqn. (1) is used to best fit the data shown in Figure 5. It is found that b increases from 0.187 to 0.320 while the initial void ratio decreases from 0.799 to 0.666 for the dry soil mixture. As expected, a dense soil has more contact points or a higher coordination number resulting in a more contribution of the effective stress on v_s. Santamarina et al. [35] reported a value of b around 0.25 for rough or angular sand and silt particles. The measured range of b for the tested soil mixture is consistent with this reference value. By adding S_h ranging between 24% and 31%, it is apparent that v_s of the hydrate bearing soil mixture is 3 to 5 times that of the host soil mixture. The increase in v_s reflects the increase in skeletal stiffness due to the presence of hydrate. Besides, b reduces to the range between 0.127 and 0.161. In other words, the hydrate bearing soil mixture is less sensitive to the effective stress. Lee et al. [32] has also observed similar trend on remould clay-dominated sediments where b decreases from 0.3 to 0.03 as S_h increases from 0 to 100%. As expected, v_s of specimen with 100% S_h (all the voids filled with THF hydrate) is almost independent of the effective stress. Furthermore, Kim et al. [33] has also obtained similar results on CO_2 hydrate bearing clayey silt where b decreases from 0.26 to 0.01 as S_h increases from 0 to 63%. It should be noted that at a S_h of 27-28% the CO_2 hydrate bearing clayey silt is less sensitive to the effective stress than the soil mixture tested in this study. The specimen preparation in this study resulted in some hydrates formed inside the intra-particle voids leading to less amount of cementation than that found in Kim et al. [33] at similar S_h.
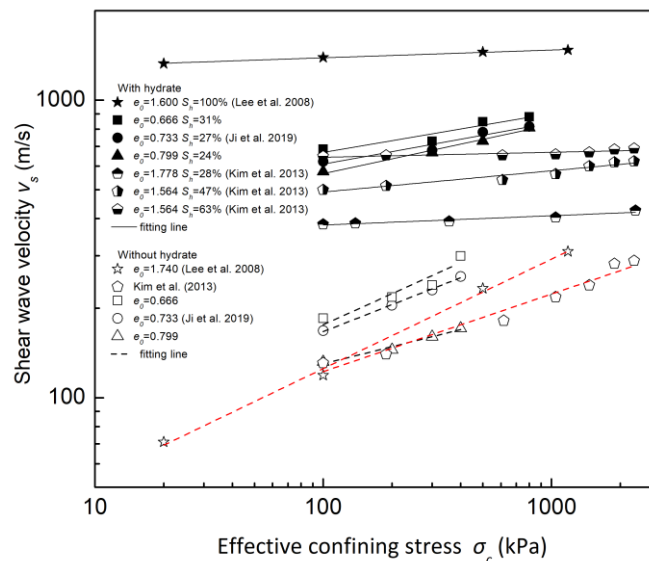

Figure 5. Comparison of shear wave velocity of CS-silt mixture with and without THF hydrate.

G_{max} is evaluated from $G_{max} = \rho v_s^2$, where ρ is soil density. Past studies [36-38] have revealed that the effective stress and void ratio are the two most important factors controlling G_{max} and the following empirical equation has been proposed:

$$G_{max} = C_0 \cdot F(e) \cdot \left(\frac{\sigma'}{P_a}\right)^h \tag{2}$$

where C_0 is a material parameter characterised by the particle size, shape, bonding and overconsolidation ratio. It increases with the increase of particle size and sphericity and roundness of particle [39]. σ' is the effective stress, $F(e)$ is a void ratio function, P_a is a reference pressure taken as 1 kPa in this study and h is the exponent term for the effective

stress. Different forms have been proposed for $F(e)$. In this study $F(e) = (0.3+0.7e^2)^{-1}$ proposed by Hardin [40] was adopted. Eqn. (2) is used to fit the measured G_{max} against the effective stress. To eliminate the influence of void ratio, Figure 6 depicts G_{max} normalised by $F(e)$ as a function of effective stress for the test results shown in Figure 5. For the hydrate bearing specimens, $F(e)$ was evaluated using effective void ratio (e'), defined as the void ratio considering hydrate as the solid constituent. It is evident from Table 2 that e' is around 57% - 64% of initial e of the host soil mixture resulting in an increase in 50% of $F(e)$ for hydrate bearing CS-silt at a S_h between 24% and 31%. As expected, the normalized G_{max} of the hydrated bearing specimens is at least one order of magnitude higher than that of the dry specimens. The best-fit values of C_0 and h and the corresponding R^2 are summarised in Table 3. The best-fit values of a hydrate bearing Leighton Buzzard Grade E (LB-E) sand using the excess gas method are also shown in the table for comparison. On the one hand, with hydrate forming in the specimens, the value of exponent h decreases from 0.57 to 0.28. The reduction in the value of h implies that the contribution of effective stress becomes less important with the addition of hydrate. In other words, the hydrate contributes to a significant part in the skeleton stiffness. On the other hand, the value of parameter C_0 increases sharply from 2 to 78, which may be due to the bonding effect of hydrate or larger and rounder coagulated particles of CS and silt bonded together by hydrate. Clayton et al. [22] studied the effects of hydrate morphology on the small-strain stiffness of the LB-E sand. Hydrate morphology is controlled by the specimen preparation method. In general, cementation hydrate morphology is formed by the excess gas method. G_{max} of hydrate bearing sand containing 10% S_h is 6 to 13 times that of the host sand as shown in Figure 6. The h value decreases from 0.42 to 0.02 and the C_0 value increases from 12 to 1394. A h value close to 0 indicates the material is either solid or cemented soil. A small amount of hydrate (low S_h) bonding the interparticle contacts is sufficient to stiffen substantially the soil matrix of host sand.
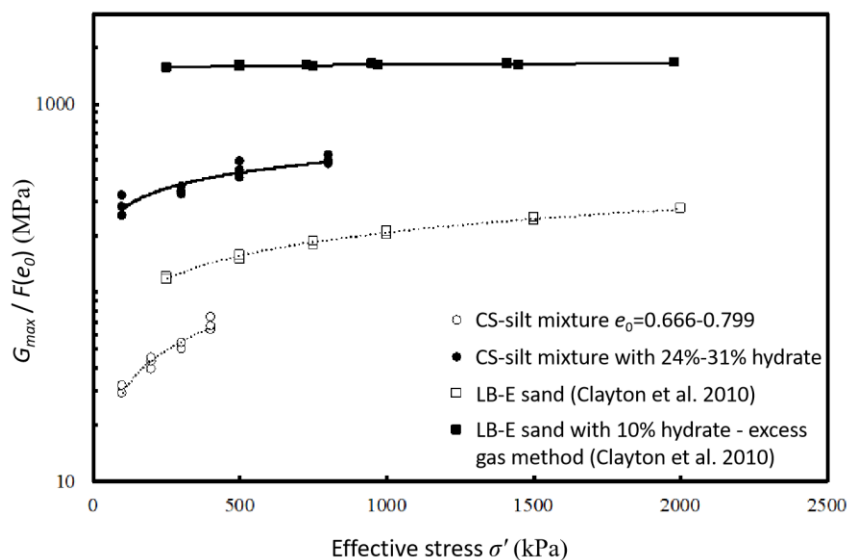
Figure 6. Relationship between normalized maximum shear modulus and effective stress.

Table 3. Best-fit values of model parameters for Eqn. (2).

Soil	C_0	h	R^2
CS-silt mixture	2	0.57	0.92
CS-silt mixture with $S_h = 24\% - 31\%$	78	0.28	0.82
LB-E sand	12	0.42	0.99
LB-E sand with $S_h = 10\%$ (excess gas method)	1394	0.02	0.76

Figure 7 compares the effects of hydrate on G_{max} of the tested soil mixture with those of two common hydrate morphologies found in sand: (i) cementation (from excess gas method) and (ii) pore-filling (from excess water method). G_{max} is normalised by the effective stress factor $(\sigma_c'/P_a)^h$ in which the exponent h is assumed as 0.5. The amount of hydrate formed in the pores of specimen is reflected by the reduction in the effective void ratio e'. It is apparent that cementation and pore-filling have the greatest and least increase in the normalized G_{max}, respectively. The hydrate bearing CS-silt mixture lies between cementation and pore-filling morphologies. Eqn. (2) with different values of C_0 are shown as broken lines in the figure. It seems that $C_0 = 6$ can be used to best fit the hydrate bearing sand with pore filling morphologies as well as the host sand. Thus, the effects of hydrate on G_{max} can be reflected by the increase in $F(e)$ as a result of the reduction in e'. On the contrary, the best-fit parameters for the hydrate bearing CS-silt are different from those of the host soil (see Table 3). It is because the accumulation of hydrates in the intra-particle voids of CS and inter-particle voids of soil mixture involves both the cementation and pore filling morphologies. Thus, all the three parameters of Eqn. (2) are affected.
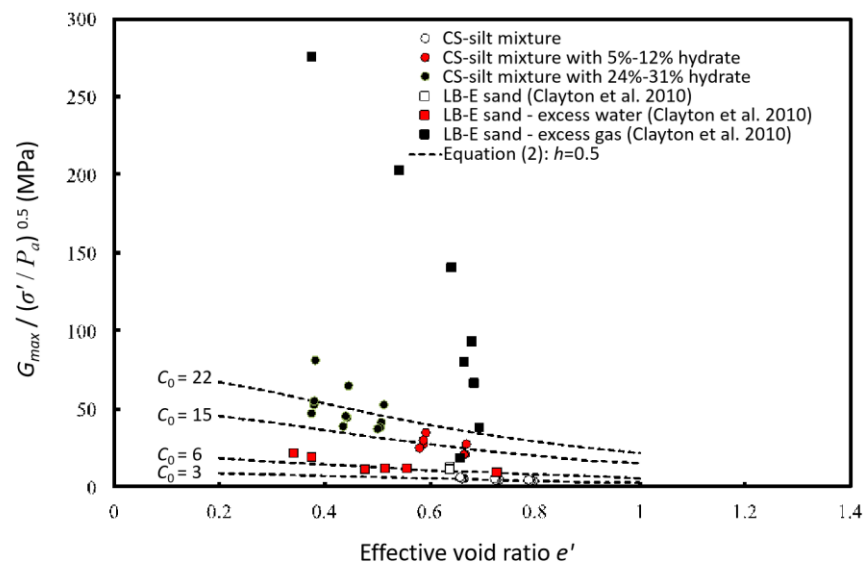

Figure 7. Relationship between normalised maximum shear modulus and effective void ratio.

To understand the effects of hydrate morphology on the soil stiffness, a frame-supporting model, namely Biot-Gassmann theory modified by Lee (BGTL) [41] and cementation model proposed by Dvorkin and Nur [42] were adopted in this study to estimate G_{max}. In the BGTL model, hydrate is assumed to be one of the solid constituents, which reduces the porosity and changes the shear modulus of the soil mixture. A reduced porosity (ϕ_r) is defined as follows:

$$\varphi_r = \varphi(1 - S_h) \tag{3}$$

where ϕ is the porosity of the soil mixture. The shear modulus of the soil mixture can be calculated from Eqn. (4) [39]:

$$G_{dry} = G_{sat} = \frac{G_{ma}K_{ma}(1-\beta)C^2(1-\varphi_r)^{2x} + G_{ma}\beta^2 M C^2(1-\varphi_r)^{2x}}{K_{ma} + 4G_{ma}\left[1 - C^2(1-\varphi_r)^{2x}\right]/3} \tag{4}$$

where G_{ma} and K_{ma} are the shear and bulk moduli of solid phase, respectively, β is a Biot coefficient, which is a function of porosity for unconsolidated sediments, x is a parame-

ter depending on the degree of consolidation and differential pressure, C is a parameter depending on clay content, M is a modulus that measures the variation in the hydraulic pressure needed to force an amount of water into the formation without any change in formation volume. The formulae used to calculate the above parameters are given in Eqns. (A1)-(A6) in the Appendix A. It should be noted fluid is not able to transmit shear waves, which has no effect on shear modulus. Therefore, $G_{dry} = G_{sat}$ in Eqn. (4).

In the cementation model [42], hydrate is assumed to form at the particle contacts. The effective bulk (K_{dry}) and shear moduli (G_{dry}) can be calculated using Eqns. (5) and (6), respectively:

$$K_{dry} = \frac{n(1-\varphi)}{6}\left(K_c + \frac{4}{3}G_c\right)S_n \tag{5}$$

$$G_{dry} = \frac{3}{5}K_{dry} + \frac{3n(1-\varphi)}{20}G_c S_T \tag{6}$$

where K_c and G_c are the bulk and shear moduli of hydrate, respectively, as shown in Table 4 [43]. S_n and S_T are parameters that are proportional to the normal and shear stresses of a pair of cemented particles, respectively, which depend on the amount of particle contacts, the soil and particle moduli. The formulae of S_n and S_T are given in Eqns. (B1) and (B2), respectively in the Appendix B [42]. n is the average number of particle contacts, taken as 5.6 in this study. Eqns. (B9) - (B17) in Appendix B [44] are used to calculate n, which agrees with the findings verified by CT that n is taken reasonably between 4.8 and 7 for random dense packing [45].

Table 4. Elastic properties of solid constituents.

Constituent	G (GPa) [43]	K (GPa) [43]
Quartz	45	36.6
Calcite	32	76.8
Hydrate	3.3	7.9

Figure 8 compares the test results with the computed values of the BGTL and cementation models for an initial void ratio of 0.733. It is apparent that the measured G_{max} of CS-silt mixture increases non-linearly from 43 to 1100 MPa for S_h ranging between 0% and 27%. The trend of non-linear increase in G_{max} with respect to S_h at low regime of S_h is consistent with the predicted tendency of the cementation model. For example, the predicted G_{max} increases from 1703 to 3565 MPa when S_h increases from 0.5% to 5%. At a low $S_h < 5\%$, certain extent of hydrate has accumulated at the inter-particle contacts in the vicinity of CS particles leading to a substantial stiffening of the soil matrix. Yu et al. [46] conducted numerical simulation on the small-strain behaviour of hydrate bearing soil using discrete element method. A contact bonding model was imposed between hydrate and soil particles to simulate the effects of cementation. The bonding effect may increase the contact number of soil matrix leading to higher shear wave velocity (or G_{max}). The numerical results showed G_{max} increases nonlinearly with S_h where the rate of increment decreases substantially with further increase in S_h. Despite a similar non-linear trend at the low regime of S_h, the magnitude of predicted G_{max} by the cementation model is much higher than the measured value. One of the limitations of the cementation model is that it is independent of effective stress. However, G_{max} is dependent on effective stress. On the other hand, BGTL model can account for the stress-dependent G_{max}. For hydrate-free soil mixture ($S_h = 0$), under an effective stress of 100 kPa and 300 kPa, BGTL predicted a G_{max} of 33 and 86 MPa, respectively, which are consistent with the test results. However,

BGTL cannot model the substantial increase in G_{max} for $0 < S_h < 5\%$. Furthermore, both of test results of Clayton et al. [22] using excess gas method and this study fall between the cementation and BGTL models. Hence, the hydrates play more than one role in soil mixture. Figure 8 also shows that for a given S_h, G_{max} of specimens prepared by excess gas method [22] is higher than that of this study. Some hydrates accumulated inside the intra-particle voids resulting in a weaker cementation effect for the CS-silt mixture, while excess gas method tend to form cementation morphology in sand enhancing significantly the stiffness of soil matrix. Thus, hydrate morphology is as important as hydrate saturation and effective stress in governing the stiffness of hydrate bearing soils.

Jung et al. [47] used discrete element method to model the stress-strain behaviour of hydrate bearing sand. Grain clusters and parallel bond model were adopted to simulate patchy hydrate and bonding effects between hydrate grains and mineral grains, respectively. The breakage of hydrate clusters was ignored in their study. According to the hypothesis shown in Figure 3, the hydrate morphology of CS-silt mixture has two distinct features: (1) filling the intra-particle and inter-particle voids, and (2) cementation at the inter-particle contacts. Due to the complex hydrate morphology, a hybrid model that incorporates features of both cementation and frame-supporting models should be used to predict the observed G_{max} of the hydrate bearing CS-silt mixture. The hydrate filled in intra-particle and inter-particle voids plays a role of frame-supporting, while the hydrate occupied the inter-particle contacts works as cementation. Various modelling techniques in discrete element method may be used to implement numerically the concept of hybrid model [46-48]. In this way, it is essential to quantify the proportions of hydrate filling the intra-particle and inter-particle voids and those cementing at the inter-particle contacts.
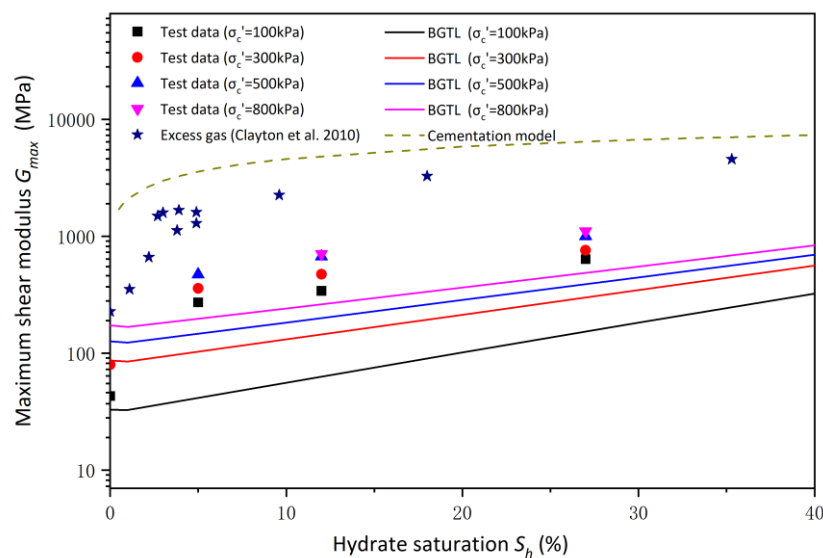
Figure 8. Relationship between maximum shear modulus and hydrate saturation.

4. Conclusions

Maximum shear modulus (G_{max}) is an important factor determining soil deformation and closely related to engineering safety and seafloor stability. Bender element test was conducted to investigate the effects of hydrate on the G_{max} of a CS-silt mixture in this study. By adopting special specimen preparation procedures, THF hydrate was formed in the intra-particle voids of CS grains and inter-particle voids between CS and surrounding silt particles. Both cementation and pore-filling hydrate morphologies contribute the skeleton stiffness of the hydrate bearing CS-silt mixture. At low hydrate satura-

tion (S_h), the cementation morphology plays a dominant role where G_{max} of the hydrate bearing CS-silt mixture increases by 4 to 6 times at a S_h of 5%. However, G_{max} also depends on the stress for the range of S_h tested. This stress-dependent stiffness implies that the hydrate with frame-supporting morphology also plays a significant role in the soil matrix. In other words, the difference of hydrate morphologies determines the effect of hydrate saturation and effective stress on hydrate bearing specimens. Therefore, neither existing cementation nor frame-supporting model, i.e. BGTL, could alone predict adequately the shear modulus of the hydrate bearing CS-silt mixture. Thus, a hybrid model incorporated both cementation and frame-supporting models should be used. This type of hybrid model may be implemented numerically using the discrete element method. Further investigation is required to provide theoretical evidence for the effects of complicated hydrate morphology on the stiffness of CS-silt mixture, which is essential for hydrate exploration and ocean engineering safety.

Author Contributions: Conceptualization, C. F. Chiu and Chao Jiang; methodology, C. F. Chiu and Chao Jiang; software, Yuzhe Ren and Chao Jiang; validation, Yuzhe Ren and Lu Ma; formal analysis, C. F. Chiu, Yuzhe Ren, Lu Ma and Y. P. Cheng; investigation, Chao Jiang; resources, Litong Ji; data curation, Yuzhe Ren and Lu Ma; writing—original draft preparation, Chao Jiang and Yuzhe Ren; writing—review and editing, C. F. Chiu and Y. P. Cheng; visualization, C. F. Chiu and Yuzhe Ren; supervision, C. F. Chiu; project administration, C. F. Chiu. All authors have read and agreed to the published version of the manuscript.

Institutional Review Board Statement: Not applicable.

Informed Consent Statement: Not applicable.

Conflicts of Interest: The authors declare no conflict of interest.

Appendix A

For Eqn (4), the shear and bulk modulus of the solid phase (G_{ma}, K_{ma}) consisting of CS, quartz silt and THF hydrate can be calculated by the average of arithmetic and harmonic means of the solid constituents [49]:

$$G_{ma} = \frac{1}{2}\left[\sum_{i=1}^{m} f_i G_i + \left(\sum_{i=1}^{m} f_i / G_i \right)^{-1} \right] \tag{A1}$$

$$K_{ma} = \frac{1}{2}\left[\sum_{i=1}^{m} f_i K_i + \left(\sum_{i=1}^{m} f_i / K_i \right)^{-1} \right] \tag{A2}$$

where m is the number of solid constituent, taken as 3. f_i, K_i and G_i are the volume fraction, bulk modulus and shear modulus of the ith solid constituent, respectively, which is taken from Table 4.

Biot coefficient (β) is given by Eqns. (A3) [41]:

$$\beta = \frac{-184.05}{1 + e^{(\varphi_r + 0.56468)/0.09425}} + 0.99494 \tag{A3}$$

The parameter C depends on clay content in sediments and exponent x are given by Eqns. (A4) and (A5), respectively:

$$C = 0.9552 + 0.0448e^{C_v/0.06714} \tag{A4}$$

$$x = \left[10^{(0.426-0.235Log_{10}P)}\right] / w \tag{A5}$$

where C_v is the clay-volume content. In this study, there is no clay-volume content in the specimen. Thus, Eqn. (A4) indicates that C equals to 1. P is the effective pressure and w is a constant which is taken as 1.2 in this study and it is suitable for unconsolidated sediments at an effective pressure less than 10 MPa [41].

The parameter M is given by (A6)

$$\frac{1}{M} = \frac{(\beta - \varphi_r)}{K_{ma}} + \frac{\varphi_r}{K_{fl}} \tag{A6}$$

where K_{fl} is the bulk modulus of fluid, which is taken as 2.18 GPa in this study.

Appendix B

For Eqns (5) and (6), the formulae of S_n and S_T are given in Eqns. (B1) and (B2), respectively:

$$S_n = -0.024153\Lambda_n^{-1.3646}\alpha^2 + 0.20405\Lambda_n^{-0.89008}\alpha + 0.000246\Lambda_n^{-1.9864} \tag{B1}$$

$$S_T = A_T(\Lambda_T, \ v)\alpha^2 + B_T(\Lambda_T, \ v)\alpha + C_T(\Lambda_T, \ v) \tag{B2}$$

$$\alpha = \left[\frac{2S_h\varphi}{3(1-\varphi)}\right]^{0.5} \tag{B3}$$

$$\Lambda_n = \frac{2G_c}{\pi G_s}\frac{(1-v_s)(1-v_c)}{1-2v_c} \tag{B4}$$

$$\Lambda_T = \frac{G_c}{\pi G_s} \tag{B5}$$

$$A_T(\Lambda_T, \ v) = -0.01(2.26v_s^2 + 2.07v_s + 2.3)\Lambda_T^{0.079v_s^2+0.1754v_s-1.342} \tag{B6}$$

$$B_T(\Lambda_T, \ v) = (0.0573v_s^2 + 0.0937v_s + 0.202)\Lambda_T^{0.0274v_s^2+0.0529v_s-0.8765} \tag{B7}$$

$$C_T(\Lambda_T, \ v) = 0.0001(9.654v_s^2 + 4.945v_s + 3.1)\Lambda_T^{0.0186v_s^2+0.401v_s-1.8186} \tag{B8}$$

where v_s and G_s are the Poisson's ratio and shear modulus of the hydrate-free soil, respectively, v_c and G_c are the Poisson's ratio and shear modulus of the hydrate, respectively. v_c is assumed as 0.15 in this study.

$$n = S_p N_{c2} + (1-S_p)N_{c1} \tag{B9}$$

$$N_{c1} = S_a N_{1,2} + (1-S_a)N_{1,1} \tag{B10}$$

$$N_{c2} = S_a N_{2,2} + (1 - S_a) N_{2,1} \tag{B11}$$

$$S_p = \frac{n_2}{n_1 + n_2} \tag{B12}$$

$$S_a = \frac{n_2 D_{p2}^2}{n_1 D_{p1}^2 + n_2 D_{p2}^2} \tag{B13}$$

$$N_{1,2} = \frac{2j\left(\dfrac{D_{p1}}{D_{p2}} + 1\right)}{1 + \dfrac{D_{p1}}{D_{p2}} - \left[\dfrac{D_{p1}}{D_{p2}}\left(\dfrac{D_{p1}}{D_{p2}} + 2\right)\right]^{1/2}} \tag{B14}$$

$$N_{2,1} = \frac{2j\left(\dfrac{D_{p2}}{D_{p1}} + 1\right)}{1 + \dfrac{D_{p2}}{D_{p1}} - \left[\dfrac{D_{p2}}{D_{p1}}\left(\dfrac{D_{p2}}{D_{p1}} + 2\right)\right]^{1/2}} \tag{B15}$$

$$N_{1,2}, \ N_{2,1} \geq 2 \tag{B16}$$

$$j = 0.067 N_c \tag{B17}$$

where, n is the average coordination number in the CS-silt mixture, $N_{1,1}$, $N_{1,2}$, $N_{2,1}$ and $N_{2,2}$ are particle 1 contacts with a reference particle 1, particle 2 contacts with a reference particle 1, particle 1 contacts with a reference particle 2 and particle 2 contacts with a reference particle 2, respectively. In this study, particle 1 refers to CS grain and particle 2 refers to silt grain. S_p is the fractional number of particles 2, and S_a is the fractional area of particles 2. D_{p1} is the diameter of particle 1, taken as 750 μm, and D_{p2} is the diameter of particles 2, taken as 43 μm from Ma et al. study [24]. It is worth noting that we assume D_{p1} and D_{p2} as D_{50} of each component in Ma et al. study. n_1 and n_2 are the number of particle 1 and particle 2, respectively, which are calculated from volume of each component by the volume of each particle. N_c is the coordination number of uniform-size spheres, taken as 6 [50]. Also, $N_{1,1}$, $N_{2,2}$ are taken as 6. It is noting that if $N_{1,2}$ and $N_{2,1}$ calculated from Eqns. (B14) and (B15) are less than 2, we take it as 2 according to Eqns. (B16). j is a proportional constant.

References

1. Waite, W.F.; Santamarina, J.C.; Cortes, D.D.; Dugan, B.; Espinoza, D.N.; Germaine, J.; Jang, J.; Jung, J.W.; Kneafsey, T.J.; Shin, H., Soga, K.; Winters, W.J.; Yun, T.S. Physical properties of hydrate-bearing sediments. *Rev. Geophys.* **2009**, *47*, RG4003. https://doi.org/10.1155/2021/6636125.
2. Dai, S.; Santamarina, J.C.; Waite W.F; Kneafsey, T.J. Hydrate morphology: Physical properties of sands with patchy hydrate saturation. *J. Geophys. Res-Sol. Ea..* **2012**, *117*, B11205. https://doi.org/10.1029/2012JB009667.
3. Lei, L.; Santamarina, J.C. Laboratory strategies for hydrate formation in fine-grained sediments. *J. Geophys. Res-Sol. Ea.* **2018**, *123*, 2583-2596. https://doi.org/10.1002/2017JB014624.
4. Argentino, C.; Conti, S.; Fioroni C.; Fontana, D. Evidences for Paleo-Gas Hydrate Occurrence: What We Can Infer for the Miocene of the Northern Apennines (Italy). Geosciences 2019, 9, 134. https://doi.org/10.3390/geosciences9030134.

5.   Hesselbo, S.P.; Grocke, D.R.; Jenkyns, H.C.; Bjerrum, C.J.; Farrimond, P.; Bell H.S.M.; Green, O.R. Massive dissociation of gas hydrate during a Jurassic oceanic anoxic event. Nature 2000, 406(6794), 392-395. https://doi.org/10.1038/35019044.

6.   Wang, X.; Collett, T.S.; Lee, M.W.; Yang, S.; Guo, Y.; Wu, S. Geological controls on the occurrence of gas hydrate from core, downhole log, and seismic data in the Shenhu area, South China Sea. *Mar. Geol*. **2014**, *357*, 272-292.   https://doi.org/10.1016/j.margeo.2014.09.040.

7.   Lei, L.; Seol, Y.; Choi J.-H.; Kneafsey, T.J. Pore habit of methane hydrate and its evolution in sediment matrix-laboratory visualization with phase-contrast micro-CT. *Mar. Petrol. Geol.* **2019**, *104*, 451-467. https://doi.org/10.1016/j.marpetgeo.2019.04.004.

8.   Lei, L.; Seol, Y. Pore-scale investigation of methane hydrate bearing sediments under triaxial condition. *Geophys. Res. Lett.* **2020**, *47(5)*, 1-11. https://doi.org/10.1029/2019GL086448.

9.   Yang, M.; Fu, Z.; Jiang, L.; Song, Y. Gas recovery from depressurized methane hydrate deposits with different water saturations. *Appl. Energ.* **2017**, *187*, 180-188. https://doi.org/10.1016/j.apenergy.2016.10.029.

10. Chong, Z.R.; Pujar, G.A.; Yang, M.J.; Linga, P. Methane hydrate formation in excess water simulating marine locations and the impact of thermal stimulation on energy recovery. *Appl. Energ.* **2016**, *177*, 409-421. https://doi.org/10.1016/j.apenergy.2016.05.077.

11. Liu, W.; Wu, Z.; Li, Y.; Song, Y.; Ling, Z.; Zhao, J.; Lv, Q. Experimental study on the gas phase permeability of methane hydrate-bearing clayey sediments. *J. Nat. Gas Sci. Eng.* **2016**, *36*, 378-384. https://doi.org/10.1016/10.1016/j.jngse.2016.10.055.

12. Wu, Z.; Li, Y.; Sun, X.; Wu, P.; Zheng, J. Experimental study on the effect of methane hydrate decomposition on gas phase permeability of clayey sediments. *Appl. Energ.* **2018**, *230*, 1304-1310. https://doi.org/10.1016/10.1016/j.apenergy.2018.09.053.

13. Li, Y.; Liu, W.; Zhu, Y.; Chen, Y.; Song, Y.; Li, Q. Mechanical behaviors of permafrost-associated methane hydrate-bearing sediments under different mining methods. *Appl. Energ* **2016**, *162*, 1627-1632. https://doi.org/10.1016/10.1016/j.apenergy.2015.04.065.

14. Song, Y.; Zhu, Y.; Liu, W.; Li, Y.; Lu, Y.; Shen Z. The effects of methane hydrate dissociation at different temperatures on the stability of porous sediments. *J. Petrol. Sci. Eng.* **2016**, *147*, 77-86. https://doi.org/10.1016/10.1016/j.petrol.2016.05.009.

15. Liu, W.; Luo, T.; Li, Y.; Song, Y.; Zhu, Y.; Liu, Y.; Zhao, J.; Wu, Z.; Xu, X. Experimental study on the mechanical properties of sediments containing CH4 and CO2 hydrate mixtures. *J. Nat. Gas Sci. Eng.* **2016**, *32*, 20-27. https://doi.org/10.1016/j.jngse.2016.03.012.

16. Yun, T.; Santamarina, J.; Ruppel, C. Mechanical properties of sand, silt, and clay containing tetrahydrofuran hydrate. *J. Geophys. Res-Sol. Ea.* **2007**, *112*, B04106. https://doi.org/10.1029/2006JB004484.

17. Zhang, X.; Lu, X.; Shi, Y.; Xia, Z.; Liu, W. Centrifuge experimental study on instability of seabed stratum caused by gas hydrate dissociation. *Ocean Eng.* **2015**, *105*, 1-9. https://doi.org/10.1016/j.oceaneng.2015.06.006.

18. Shi, Y.; Zhang, X.; Lu, X.; Wang, S.; Wang, A. Experimental study on the static mechanical properties of hydrate-bearing silty-clay in the South China Sea. *Chinese Journal of theoretical and applied mechanics* **2015**, *47(3)*, 521-528. https://doi.org/10.6052/0459-1879-14-424.

19. Hyodo, M.; Yoneda, J.; Yoshimoto, N.; Nakata, Y. Mechanical and dissociation properties of methane hydrate-bearing sand in deep seabed. *Soils Found*. **2013**, *53*, 299–314. https://doi.org/10.1016/j.sandf.2013.02.010.

20. Liu, Z.; Kim, J.; Hu, G.; Hu, W.; Ning, F. Geomechanical property evolution of hydrate-bearing sediments under dynamic loads: Nonlinear behaviors of modulus and damping ratio. *Eng. Geol.* **2021**, *295*, 106427. https://doi.org/10.1016/j.enggeo.2021.106427.

21. Liu W.; Liu R.; Zhang M.; Liu Z.; Lang C.; Li Y. Rheological properties of hydrate slurry formed from mudflows in South China Sea. Energ. Fuel. **2021**, 35, 10575-10583. https://doi.org/10.1021/acs.energyfuels.1c01294.

22. Clayton C.R.I.; Priest J.A.; Rees E.V.L. The effects of hydrate cement on the stiffness of some sands. *Geotechnique* **2010**, *60*, 435-445. https://doi.org/10.1680/geot.2010.60.6.435.

23. Liu, C.; Ye, G.; Meng, Q.; He, X.; Lu, H.; Zhang, J.; Liu, J.; Yang, S. The characteristics of gas hydrates recovered from Shenhu Area in the South China Sea. *Mar. Geol.* **2012**, *307*, 22-27. https://doi.org/10.1016/j.margeo.2012.03.004.

24. Ma, L.; Chiu, C.F.; Cheng, Y.P.; Ren, Y.Z. Effects of particle breakage on the compression behaviour of gap graded carbonate sand–silt mixtures. *Geotechnique Lett*. **2021**, *10*, 1-5. https://doi.org/10.1680/JGELE.20.00033.

25. Yun, T.S.; Francisca, F.M.; Santamarina, J.C.; Ruppel, C. Compressional and shear wave velocities in uncemented sediment containing gas hydrate. *Geophys. Res. Lett.* **2005**, *32*, L10609. https://doi.org/10.1029/2005GL022607.

26. Mahabadi, N.; Zheng, X.; Jang, J. The effect of hydrate saturation on water retention curves in hydrate-bearing sediments. *Geophys. Res. Lett.* **2016**, *43(9)*, 4279-4287. https://doi.org/10.1002/2016GL068656.

27. Nikitin, V.V.; Dugarov, G.A.; Duchkov, A.A.; Fokin, M.I.; Drobchik, A.N.; Shevchenko, P.D.; De Carlo, F.; Mokso, R. Dynamic in-situ imaging of methane hydrate formation and self-preservation in porous media. *Mar. Petrol. Geol.* **2020**, *115*, 104234. https://doi.org/10.1016/j.marpetgeo.2020.104234.

28. Li, C.; Hu, G.; Zhang, W.; Ye, Y.; Liu, C.; Li, Q.; Sun, J. Influence of foraminifera on formation and occurrence characteristics of natural gas hydrates in fine-grained sediments from Shenhu area, South China Sea. *Science China-Earth Sciences*, **2016**, 46(9),1223-1230. https://doi.org/10.1007/s11430-016-5005-3.

29. Ji, L.; Chiu, A.C.F.; Ma, L.; Jian, C. Shear modulus of hydrate bearing calcareous sand-fines mixture. *EWeb of Conferences* **2019**, *92*, 04002. https://doi.org/10.1051/e3sconf/20199204002.

30. Cheng Z.; Leong E.C. Determination of damping ratios for soils using bender element tests. *Soil Dyn. Earthq. Eng.* **2018**, *111*, 8-13. https://doi.org/10.1016/j.soildyn.2018.04.016.

31. Sodeifian G. Non-Linear Rheology of Polymer Melts. *LAP Lambert Acad. Publ.*, 2011.

32. Lee J.Y.; Santamarina J.C.; Ruppel C. Mechanical and electromagnetic properties of northern Gulf of Mexico sediments with and without THF hydrates. *Mar. Petrol. Geol*. **2008**, *25*, 884-895. https://doi.org/10.1016/j.marpetgeo.2008.01.019.

33. Kim, H.; Cho, G.; Kwon, T. Effect of CO_2 hydrate formation on seismic wave velocities of fine-grained sediments. Geochem. Geophy. Geosy. 2013, 14, 1787-1799. https://doi.org/10.1002/ggge.20102

34. Hardin B.O.; Richart Jr. F.E. Elastic Wave Velocities in Granular Soils. *J. Geotech. Geoenviron*. **1963**, *89*, 33-65. https://doi.org/10.1061/JSFEAQ.0000493.

35. Santamarina J.C.; Klein, K.A.; Fam, M.A. Soils and waves: Particulate materials behavior, characterization and process monitoring. *J. Soil. Sediments*. **2001**, *1*, 130. https://doi.org/10.1007/BF02987719.

36. Hardin, B.O.; Blandford, G.E. Elasticity of particulate materials. *J. Geotech. Eng., ASCE*, **1989**, *115*, 788-805. https://doi.org/10.1061/(ASCE)0733-9410(1989)115:6(788).

37. Jamiolkowski, M.; Lancellotta, R; Lo Presti, D.C.F. Remarks on the stiffness at small strains of six Italian clays. *Pre-failure Deformation of Geomaterials 1994*, 2, 817-836.

38. Stokoe, K.H.II.; Darendeli, M.B.; Andrus, R.D.; Brown, L.T. Dynamic soil properties: Laboratory, field and correlation studies, theme lecture. In Proceedings of 2nd International Conference on Earthquake Geotechnical Engineering, Lisbon, Portugal, 1999.

39. Bui, M.T. Influence of some particle characteristics on the small strain response of granular materials. University of Southampton, PhD thesis, 2009.

40. Hardin, B.O. The nature of stress-strain behaviour of soils. In Proceedings of ASCE Geotechnical Engineering Division Speciality Conference, Pasadena, US, June 1978. https://doi.org/10.1016/0167-8760(91)90039-Z.

41. Lee, M.W. Elastic properties of overpressured and unconsolidated sediments. U.S.Geological Survey Bulletin 2214. 2003. https://doi.org/10.3133/b2214.

42. Dvorkin, J.; Nur, A. Rock Physics for Characterization of Gas Hydrates. in The Future of Energy Gases, US Geological Survey Professional Paper, **1993**, 1570, 293-298.

43. Helgerud, M.B.; Dvorkin, J.; Nur, A.; Sakai, A.; Collett, T. Elastic-wave velocity in marine sediments with gas hydrates: effective medium modeling. *Geophys. Res. Lett*. **1999**, *26(13)*, 2021-2024. https://doi.org/10.1029/1999GL900421.

44. Suzuki, M.; Oshima, T. Estimation of the co-ordination number in a multi-component mixture of spheres. *Power Technology* **1983**, *35*, 159-166. https://doi.org/10.1016/0032-5910(83)87004-1.

45. Schmidt, J.; Parteli, E.J.R.; Uhlmann, N.; Wörlein, N.; Wirth, K.-E.; Pöschel, T.; Peukert, W. Packings of micron-sized spherical particles-Insights from bulk density determination, X-ray microtomography and discrete element simulations. *Adv. Powder Technol*. **2020**, *31(6)*, 2293-2304. https://doi.org/10.1016/j.apt.2020.03.018.

46. Yu, Y.; Xu, X.; Cheng, Y.P.; Soga, K. Study on small-strain behaviours of methane hydrate sandy sediments using discrete element method. *Powders and Grains 2013*, **2013**, *1542(1)*, 555-558. https://doi.org/10.1063/1.4811991.

47. Jung, J.-W.; Santamarina, J.C.; Soga, K. Stress-strain response of hydrate-bearing sands: Numerical study using discrete element method simulations. *Geophys. Res-Sol. Ea*. **2012**, *117(4)*, B04202. https://doi.org/10.1029/2011JB009040.

48. Zhu, H.P.; Zhou, Z.Y.; Yang, R.Y.; Yu, A.B. Discrete particle simulation of particulate systems: A review of major applications and findings. *Chem. Eng. Sci*. **2009**, *63(23)*, 5728-5770. https://doi.org/10.1016/j.ces.2008.08.006.

49. Hill, R. The elastic behaviour of a crystalline aggregate. *Proc. of the phys. Soc. A*. **1952**, *65*, 349-354. https://doi.org/10.1088/0370-1298/65/5/307.

50. Suzuki, M.; Oshima, T. Co-ordination number of a multi-component randomly packed bed of spheres with size distribution. *Power Technology* **1985**, *44*, 213-218. https://doi.org/10.1016/0032-5910(85)85002-6.